X-ray absorption and resonant Auger spectroscopy of O2 in the vicinity of the O 1s →σ* resonance: Experiment and theory

著者	Feifel R., Velkov Y., Carravetta V., Angeli C., Cimiraglia R., Salek P., Gel'mukhanov F., Sorensen S. L., Piancastelli M. N., Fanis A. De, Okada K., Kitajima M., Tanaka T., Tanaka H., Ueda K.
journal or publication title	Journal of Chemical physics
volume	128
number	6
page range	064304
year	2008
URL	http://hdl.handle.net/10097/52445

doi: 10.1063/1.2831920

X-ray absorption and resonant Auger spectroscopy of O_2 in the vicinity of the O $1s \rightarrow \sigma^*$ resonance: Experiment and theory

R. Feifel,[1,a)] Y. Velkov,[2] V. Carravetta,[3] C. Angeli,[4] R. Cimiraglia,[4] P. Sałek,[2] F. Gel'mukhanov,[2] S. L. Sorensen,[5] M. N. Piancaśtelli,[1] A. De Fanis,[6] K. Okada,[7] M. Kitajima,[8,b)] T. Tanaka,[8] H. Tanaka,[8] and K. Ueda[9]
[1]*Department of Physics, Uppsala University, Box 530, S-751 21 Uppsala, Sweden*
[2]*Department of Theoretical Chemistry, Roslagstullsbacken 15, Royal Institute of Technology, S-106 91 Stockholm, Sweden*
[3]*Institute of Chemical Physical Processes—CNR, via Moruzzi 1, 56124, Pisa, Italy*
[4]*Department of Chemistry, University of Ferrara, via Borsari 46, 44100 Ferrara, Italy*
[5]*Department of Synchrotron Radiation Research, Institute of Physics, University of Lund, Box 118, S-221 00 Lund, Sweden*
[6]*Japan Synchrotron Radiation Research Institute, Sayo-gun, Hyogo 679-5198, Japan*
[7]*Department of Physical Science, Hiroshima University, 1-3-1 Kagamiyama, Higashi-Hiroshima, 739-8526 Japan*
[8]*Department of Physics, Sophia University, Tokyo 102-8554, Japan*
[9]*Institute of Multidisciplinary Research for Advanced Materials, Tohoku University, 2-1-1 Katahira, Aoba-ku, Sendai, 980-8577 Japan*

(Received 5 November 2007; accepted 14 December 2007; published online 11 February 2008)

We report on an experimental and theoretical investigation of x-ray absorption and resonant Auger electron spectra of gas phase O_2 recorded in the vicinity of the O $1s \rightarrow \sigma^*$ excitation region. Our investigation shows that core excitation takes place in a region with multiple crossings of potential energy curves of the excited states. We find a complete breakdown of the diabatic picture for this part of the x-ray absorption spectrum, which allows us to assign an hitherto unexplained fine structure in this spectral region. The experimental Auger data reveal an extended vibrational progression, for the outermost singly ionized $X\,^2\Pi_g$ final state, which exhibits strong changes in spectral shape within a short range of photon energy detuning ($0\ \text{eV} > \Omega > -0.7\ \text{eV}$). To explain the experimental resonant Auger electron spectra, we use a mixed adiabatic/diabatic picture selecting crossing points according to the strength of the electronic coupling. Reasonable agreement is found between experiment and theory even though the nonadiabatic couplings are neglected. The resonant Auger electron scattering, which is essentially due to decay from dissociative core-excited states, is accompanied by strong lifetime-vibrational and intermediate electronic state interferences as well as an interference with the direct photoionization channel. The overall agreement between the experimental Auger spectra and the calculated spectra supports the mixed diabatic/adiabatic picture. © *2008 American Institute of Physics*. [DOI: 10.1063/1.2831920]

I. INTRODUCTION

The *K*-shell photoabsorption spectrum of O_2 has been the subject of numerous investigations (see Refs. 1–17). The comparatively large number of studies can be understood on the grounds of the complexity of an open-shell molecule, and of the presence of several bound and dissociative states. Whereas the O $1s \rightarrow \pi^*$ resonance, located at ~530.8 eV photon energy, reflects a comparatively simple and well understood vibrational fine structure,[11] the region between ~535 and ~545 eV is a challenge to interpret since there are overlapping states converging to both the $^4\Sigma_u^-$ and $^2\Sigma_u^-$ core-hole states at 543.39 and 544.43 eV.[18] There is also an underlying Rydberg-valence mixing[5,8,9,12,15] which further complicates the interpretation, as evidenced by the controversy concerning the energy splitting of triplet states in the absorption spectrum.[2–8] This controversy was resolved by a detailed study which used the electronic decay to final electronic states to separate the two components.[12] In some of the earlier studies,[6,10,12,14,16,17] this part of the x-ray absorption spectrum was investigated using resonant Auger electron spectroscopy for probing the core-excited states. In this way, the valence character of O $1s \rightarrow$ Rydberg excited O_2 could be confirmed in a more direct way.[12,14,17]

Following the line of the scattering experiments mentioned above, we use soft x-rays to excite the O $1s \rightarrow \sigma^*$ resonance, and analyze the experimental resonant Auger spectra using wave-packet dynamics simulations. In particular, we measure the extended vibrational progression of the $X\,^2\Pi_g$ final ionic state populated through scattering in the O $1s$ core-excited states. The potential energy curves of such states are often dissociative which can lead to a variety of effects, and molecular oxygen has been a showcase of new effects such as ultrafast dissociation, Doppler split atomic lines, and localization effects.[19–23] The electronic interaction

a)Electronic mail: raimund.feifel@fysik.uu.se.
b)Present address: Department of Chemistry, Tokyo Institute of Technology, Tokyo 152-8551, Japan.

between close-lying diabatic states may lead to avoided curve crossings and to the breakdown of the Born-Oppenheimer approximation, due to nonadiabatic vibronic coupling (VC), which is known to affect x-ray absorption spectra (XAS),[24] x-ray photoionization,[24,25] and resonant x-ray raman scattering[19,26,27] spectra. We find that the x-ray absorption spectrum is influenced strongly by avoided curve crossings of six close-lying core-excited states. The Auger electron spectra show a peculiar interference pattern in the vibrational intensity distribution; our simulations confirm that this is due to interference between the resonant and direct photoionization channels. As a consequence of lifetime-vibrational interference[19,30] also channel-channel interference, i.e. interference due to the interaction of different intermediate states, is found.

II. EXPERIMENT

The experiments were performed at the *c* branch of the photochemistry beamline 27SU (Ref. 31) at SPring-8, Japan. This beamline uses a figure-8 undulator[32,33] as light source and is equipped with a high-resolution varied line-spacing monochromator.[34] The polarization vector $\mathcal{E}$ of the undulator light may be set horizontal (first harmonic) or vertical (0.5th harmonic) at this beamline.[32,33] The electron spectra were measured with a commercially available high-resolution photoelectron spectrometer (Gammadata Scienta SES-2002) equipped with a gas cell. The spectrometer lens axis lies in the horizontal direction, perpendicular to the photon beam direction.[35] In this arrangement, the electron spectra recorded with horizontal and vertical polarization correspond to the electron emission parallel and perpendicular to the $\mathcal{E}$ vector. The photon flux normalization is made by two drain currents on the last refocusing mirror and after the gas cell. All electron spectra are normalized to the acquisition time, the gas pressure, and the photon flux. Spectra corrected for anisotropic electron emission were constructed by combining the 0° and 90° spectra measured at the same photon energy according to

$$I(54.7^\circ) = I(0^\circ) + 2 \times I(90^\circ). \quad (1)$$

The degree of linear polarization was found in a previous study to be larger than 0.98 for the current optical settings,[36] which justifies the underlying assumption of Eq. (1) of completely linearly polarized light. The monochromator band pass was set to 70 meV full width at half maximum, the electron spectrometer band pass to 63 meV and the inhomogeneous Doppler broadening due to thermal motion of the sample molecules is estimated to be around 50 meV, resulting in a total experimental line width for the electron spectra of around 110 meV.

The absolute photon energy scale was established with an accuracy of ±40 meV by measuring the total ion yield (TIY) with a 4π sr detector[37] and by using the literature value of the $4p\sigma$ $(^4\Sigma_u^-)$ $v=0$ state provided by Hitchcock and Brion[1] as reference. The monochromator bandwidth was set to around 30 meV for the TIY measurement. The absorption spectrum is corrected for variations in the gas pressure and the photon flux. The electron spectra are calibrated using the

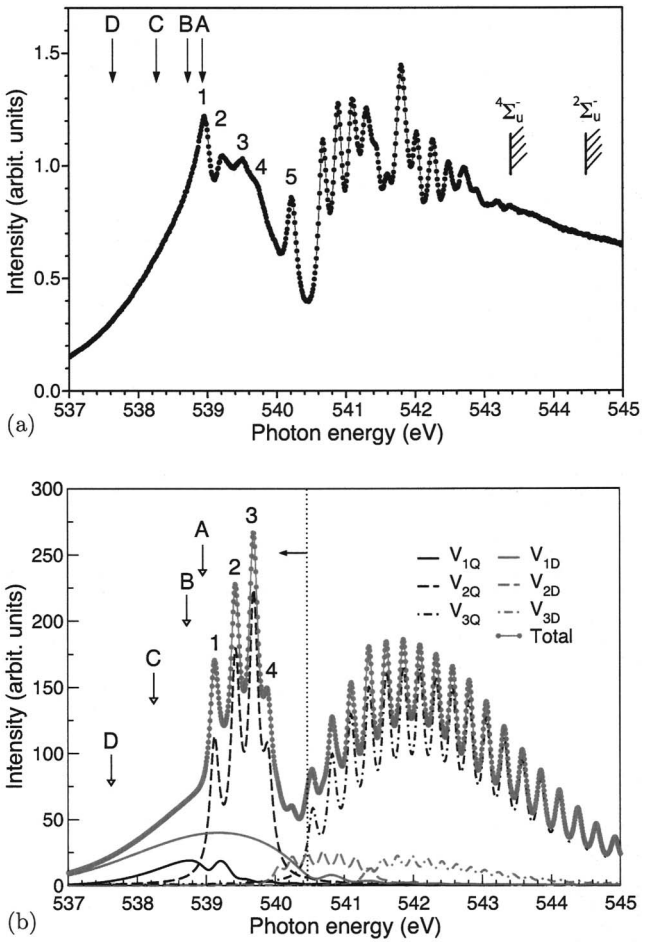

FIG. 1. (a) Experimental x-ray absorption spectrum of O_2 recorded in the vicinity of the O 1*s* ionization threshold. Photon energies used for the recording of resonant Auger electron spectra are marked by arrows and labeled A, B, C, and D, respectively. The absolute energy scale has been established according to Ref. 1; (b) theoretical x-ray absorption spectrum calculated by the four-crossing model (see text for further details). The absolute theoretical energy scale was shifted by about +1.0 eV in order to match the experimental spectrum.

$X\,^2\Pi_g$ $(v=0)$ state binding energy of 12.074 eV as reference.[38] O_2 gas was commercially obtained with a stated purity of >99.99%.

III. RESULTS

In Fig. 1(a) we show the high-resolution oxygen *K*-edge total ion yield XAS of O_2 recorded in the photon energy range between 537 and 545 eV. The two O 1*s* ionization thresholds $^4\Sigma_u^-$ and $^2\Sigma_u^-$ at 543.39 and 544.43 eV (Ref. 18) are indicated in the plot. Similar spectra are found in the literature but the sharp peaks labeled 1–4 have not been as clearly resolved in earlier works.[5,8,12,15] The interpretation of the features in the absorption spectrum is based on *ab initio* calculations of the bound Rydberg and dissociative potentials in the region. These core-excited states involve the virtual σ^*, 3*s*, and 3*p* orbitals converging to both the quartet and doublet states. The theoretical treatment of the XAS, which results are partially shown in Fig. 1(b) and which we will discuss in further detail below, aims primarily to identify the sharp features in the spectrum below 540.5 eV photon energy, and to understand the underlying mechanisms which

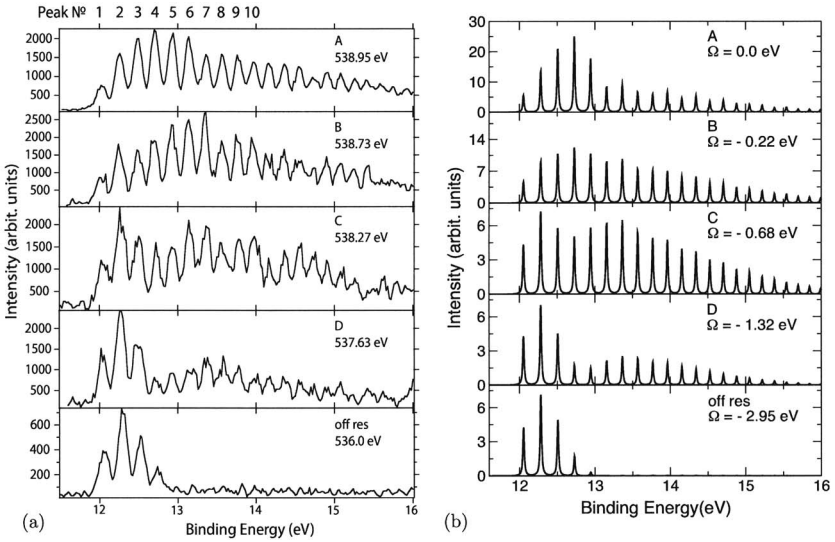

FIG. 2. (a) Experimental resonant Auger electron spectra of O_2 for excitation energies marked by arrows in Fig. 1(a); (b) theoretical resonant Auger spectra calculated by the four-crossing model (see text for further explanations); the direct channel is included with $A=60$ and $\phi=100°$.

are important for the general features of the XAS. A detailed understanding of the features 1–4 is crucial in order to interpret properly resonant Auger electron spectra which we recorded originally in this excitation region for photon frequency detunings as indicated by arrows in Fig. 1(a) and labeled A, B, C, D, and "off res" in what follows.

Figure 2(a) shows the 11.5–16 eV binding energy region of this series of resonant Auger electron spectra. They reflect a highly resolved vibrational structure associated with the outermost singly ionized $X\ ^2\Pi_g$ state of O_2. There are two distinctive features in these spectra. The first one is the extended vibrational band with up to at least 20 vibrational sublevels observed at various photon energies, and the second one is the high sensitivity of the spectral shape to the photon energy detuning Ω. As we can see, within a comparatively short range of detuning ($0\ \text{eV} > \Omega > -0.7\ \text{eV}$), the experimental spectra exhibit strong changes in shape. In spectrum A, the maximum intensity is located around peaks 4 and 5, in spectrum B this maximum is shifted to peaks 6 and 7, and in spectrum C the enhanced peak 2 is followed by a distinct dip in the region of peaks 3, 4, and 5. At a photon energy detuning of −2.95 eV below peak 1, large parts of the vibrational progression have disappeared, and the spectrum essentially reflects the direct photoionization channel; we therefore refer to it as the off resonance ("off res") spectrum in what follows. In order to get a better understanding of the experimental observations, we attempted to reproduce this spectral behavior by resonant Auger electron scattering (RAS) wave-packet dynamic simulations, some of which are displayed in Fig. 2(b) and which we will discuss also in more detail in what follows.

We would like to mention that atomic spectral features due to ultrafast dissociation, which have previously been examined in detail in this excitation energy region (see, e.g., Refs. 19 and 21 and references therein), show up at apparently higher binding energies (BE > 16 eV) than studied here and, hence, do not need to be considered further in the present context.

IV. THEORETICAL FRAMEWORK

Motivated by the experimental investigations, we studied theoretically the resonant Auger scattering process from the neutral ground state,

$$^3\Sigma_g^-: 1\sigma_g^2 1\sigma_u^2 2\sigma_g^2 2\sigma_u^2 3\sigma_g^2 1\pi_u^4 1\pi_g^2, \tag{2}$$

to the outermost singly ionized final state,

$$X^2\Pi_g: 1\sigma_g^2 1\sigma_u^2 2\sigma_g^2 2\sigma_u^2 3\sigma_g^2 1\pi_u^4 1\pi_g^1, \tag{3}$$

via six intermediate core-excited states associated with the promotion of the O $1s$ electron to three virtual orbitals,

$$\text{O } 1s \rightarrow \sigma^*, 3s, 3p. \tag{4}$$

The resonant Auger scattering is expected to be accompanied by direct ionization of the $1\pi_g$ electron. We first identify the most important scattering channels and determine which treatment of curve crossing best explains the measured x-ray absorption spectrum.

A. Mixed adiabatic/diabatic representation

We carried out *ab initio* calculations[39] of six mutually crossing diabatic potential curves corresponding to two dissociative states σ^*(D) and σ^*(Q), and four slightly-bound Rydberg states $3s$(D), $3s$(Q), $3p$(D), $3p$(Q). The labels D, Q identify the spin character (D=doublet, Q=quartet) of the ionic configuration corresponding to the largest configurational contribution to the triplet core-excited state. As the spin character is highly important in the interaction between states, we adopt this "orbital (ion spin coupling)" label. The complexity of this set of potential curves and their interactions demands a careful treatment; in particular, the interpotential crossings are crucial.

The crossing between two potential curves can be treated in the diabatic limit or in the adiabatic limit. The diabatic states are by definition not eigenstates of the total electronic Hamiltonian and are only weakly dependent on the nuclear geometry. If the crossing is treated in the diabatic limit, then a strict wave-packet technique must take the interstate coupling due to the electronic Hamiltonian (also called Coulomb

TABLE I. Calculated electronic interaction β of different core-excited states at the corresponding crossing points (in a.u.). Crossings between Rydberg states are not included.

	$3p$(D)	$3s$(D)	$3p$(Q)	$3s$(Q)
σ^*(D)	**−0.0256**	**+0.0030**	+0.0001	−0.0008
σ^*(Q)	+0.0005	−0.0007	**−0.0282**	**+0.0034**

coupling in the following) into account; this is represented by the electronic matrix element between two diabatic states, β, at the crossing point. The adiabatic states, which are eigenstates of the total electronic Hamiltonian, exhibit an avoided crossing with splitting 2β. This case constitutes a breakdown of the Born-Oppenheimer approximation, making nonadiabatic VC between the states important. There is a link between the Coulomb interaction and the nonadiabatic vibronic coupling: The smaller the splitting 2β, the larger the vibronic coupling and approaches based on the Hamiltonians $H_{\mathrm{diab}}+V_e$ and $H_{\mathrm{adiab}}+V_{\mathrm{VC}}$ should lead to the same final result. Here, V_e and V_{VC} are electronic and nonadiabatic coupling operators, respectively. Thus, if a crossing between two diabatic states with negligible β is represented in its adiabatic limit, there will be a large vibronic coupling which will act as a "force" restoring the diabatic picture.

We treat the crossings diabatically or adiabatically depending upon the magnitude of β at each particular crossing (see Table I),

$$\beta(i|j) = \langle i|H|j\rangle,$$
$$i \neq j = \sigma^*(\mathrm{Q}), 3p(\mathrm{Q}), 3s(\mathrm{Q}), \sigma^*(\mathrm{D}), 3p(\mathrm{D}), 3s(\mathrm{D}). \tag{5}$$

In particular, the crossing point is treated diabatically if the magnitude of the electronic coupling parameter, $|\beta|$, is smaller than a threshold value, β_c, and adiabatically if $|\beta|$ is greater than the threshold.

We consider three distinct models based on the value of the threshold β_c:

- $\beta_c=\infty$—the *diabatic* model;
- $\beta_c=0.025$ a.u.—the *two-crossing* model;
- $\beta_c=0.0025$ a.u.—the *four-crossing* model.

It is important to note that states of the same "multiplicity" (α=Q or D) interact more strongly and the largest coupling $\beta(i|j)$ occurs between states $\sigma^*(\alpha)$ and $3p(\alpha)$ (see Table I) as was recognized earlier.[8,14,15] The diabatic model neglects electronic interaction between states. According to Table I the two-crossing model treats crossings between σ^*(D) and $3p$(D), and between σ^*(Q) and $3p$(Q) adiabatically, while the remaining crossings are treated in the diabatic limit. The four-crossing model treats the four crossings between σ^*(D) and $3p$(D), between σ^*(D) and $3s$(D), between σ^*(Q) and $3p$(Q), and between σ^*(Q) and $3s$(Q) adiabatically (see Table I). It is of interest to analyze the determination of the mixed set of adiabatic/diabatic potential curves from the diabatic curves in the four-crossing model in further detail. The potentials of the two-crossing model are obtained by the same "adiabatization-of-the-crossings" procedure as used for the four-crossing model, but only the σ^*(D), $3p$(D), σ^*(Q), and $3p$(Q) states are included.

According to the previous discussion, the six original diabatic states can be divided into two subgroups (α=D,Q), since only states of the same "multiplicity" (i.e., more correctly, corresponding to the same spin coupling of the ionic state) have $\beta > \beta_c = 0.0025$ a.u. (see Table I). The construction of adiabatic states is then separated into two independent eigenvalue problems,

$$\psi_{i\alpha} = c_{i,\sigma^*(\alpha)}\psi_{\sigma^*(\alpha)} + c_{i,3p(\alpha)}\psi_{3p(\alpha)} + c_{i,3s(\alpha)}\psi_{3s(\alpha)},$$
$$i = 1,2,3, \quad \alpha = \mathrm{D},\mathrm{Q}; \tag{6}$$

where i runs over the new adiabatic states. The off-diagonal elements of the electronic matrix are $\beta(\sigma^*(\alpha)|3p(\alpha))$, $\beta(\sigma^*(\alpha)|3s(\alpha))$, $\beta(3s(\alpha)|3p(\alpha))=0$.

The character of the adiabatic curves can be assigned according to the character of their parent diabatic curves at the ground-state equilibrium bond distance: $V_{1\mathrm{Q}}$, $V_{2\mathrm{Q}}$, $V_{3\mathrm{Q}}$ (Q subgroup), $V_{1\mathrm{D}}$, $V_{2\mathrm{D}}$, $V_{3\mathrm{D}}$ (D subgroup). In the same way, the "parent" diabatic states determine the character of the new states: $\sigma^*(\alpha)\rightarrow V_{1\alpha}$, $3s(\alpha)\rightarrow V_{2\alpha}$, $3p(\alpha)\rightarrow V_{3\alpha}$ (α=D,Q). Once the mixing coefficients of Eq. (6) are defined, the calculation of the transition matrix elements of the core excitation and Auger decay can be carried out,

$$d_{i\alpha}^{\mathrm{ad}}(R) = \sum_n c_{i,n(\alpha)}(R) d_{n(\alpha)}^{\mathrm{diab}}(R),$$
$$Q_{i\alpha}^{\mathrm{ad}}(R) = \sum_n c_{i,n(\alpha)}(R) Q_{n(\alpha)}^{\mathrm{diab}}(R), \tag{7}$$
$$n(\alpha) = \sigma^*(\alpha), 3s(\alpha), 3p(\alpha).$$

Here, $d_{i,\alpha}^{\mathrm{ad}}(R)$ and $Q_{i,\alpha}^{\mathrm{ad}}(R)$ are the adiabatic matrix elements of the transition dipole moments and of the Coulomb decay transition [see Figs. 3(a) and 3(b)], and $d_{i,n(\alpha)}^{\mathrm{diab}}(R)$ and $Q_{i,n(\alpha)}^{\mathrm{diab}}(R)$ are the original diabatic matrix elements (see Table II).[39]

The R dependence of the adiabatic dipole moments is another factor considered in this analysis. In Table I we see that $\beta(\sigma^*(\mathrm{Q})|3p(\mathrm{Q})) > \beta(\sigma^*(\mathrm{Q})|3s(\mathrm{Q}))$, and the state $V_{3\mathrm{Q}}$ has smoothly varying dipole moments $d_{i,\alpha}^{\mathrm{ad}}(R)$ and $Q_{i,\alpha}^{\mathrm{ad}}(R)$ while the matrix elements of state $V_{1\mathrm{Q}}$ vary more dramatically with R [cf. Figs. 3(a) and 3(b)]. On this basis, we expect the error generated by noncoupled wave-packet propagation to be much larger for $V_{1\mathrm{Q}}$ than for $V_{3\mathrm{Q}}$.

In the interest of clarity, we define a notation for the adiabatic states of the two-crossing model with parent states at R=2.6 a.u. as follows: $\sigma^*(\alpha)\rightarrow V'_{1\alpha}$, $3p(\alpha)\rightarrow V'_{2\alpha}$ (α=D,Q), where the prime indicates states belonging to the two-crossing model.

B. Electronic state calculations

The core-excited states are considered to be quasistationary states embedded in the electronic continuum and their calculation by standard quantum chemical methods requires particular care to prevent variational collapse to lower excited states. We performed extensive multireference CI cal-

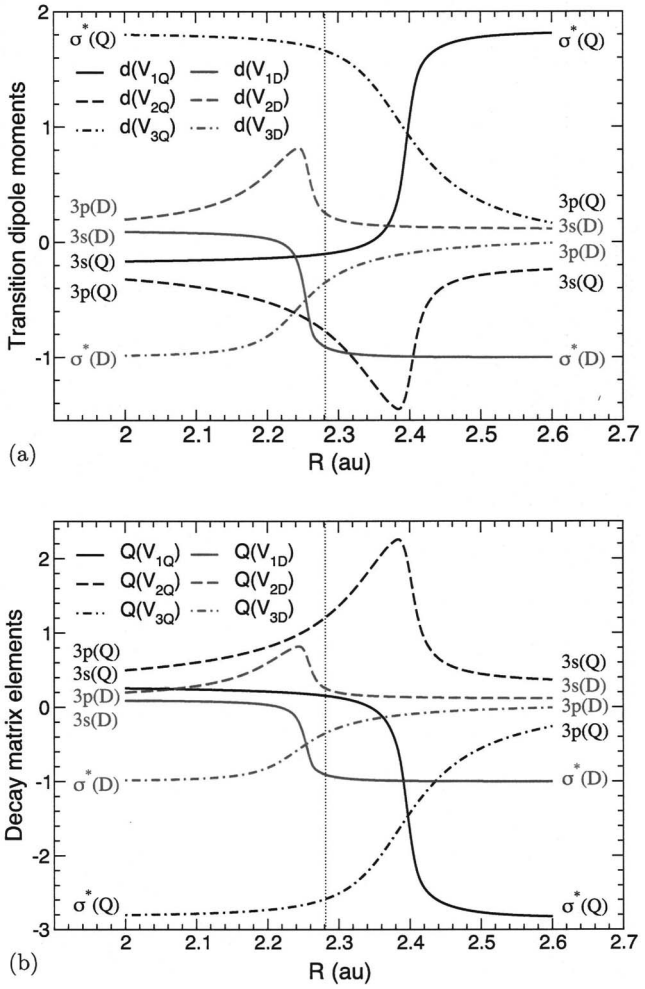

FIG. 3. (a) Transition dipole moment matrix elements based on the potential curves from Fig. 4(b) (four-crossing model); (b) Decay matrix elements based on the potential curves from Fig. 4(b) (four-crossing model). The vertical dotted line indicates R_{eq} of the ground state.

culations at different interatomic distances in order to obtain accurate potential curves for the nuclear dynamics calculations. In the independent-particle approximation, excitation of one electron from a core orbital to a virtual orbital leads to two dipole-allowed $^3\Sigma_u^-$ core-excited states. Calculations of a number of $^3\Sigma_u^-$ core-excited states, covering an excitation energy range of about 4 eV, by multireference configuration interaction (CI) using the configuration interaction by perturbation with multiconfigurational zeroth-order wavelength selected by iterative process method with aimed selection[40,41] have been carried out as described in more details in Ref. 39. The lowest 25 core-excited states have been computed at different internuclear distances R in the range $R=2.0-2.6$ a.u. around the ground-state equilibrium geometry ($R_{eq}=2.28$ a.u.). A unique CI space of about 80 000 determinants, deriving from the union of the optimized CI spaces obtained at a number of internuclear distances, was used for all geometries in order to avoid discontinuities in the potential energy curves. A diabatization method[42,43] based on a unitary transformation of the adiabatic wavefunctions, by imposing the condition of maximum squared overlap between diabatic states and "reference states," was employed. The reference states were chosen as the linear combinations of the four main determinants sharing a given orbital excitation and differing only in the spin couplings of the unpaired electrons.[14]

TABLE II. Ratio between the matrix elements of the dipole moment and the decay operator of the diabatic core-excited states, computed at the ground-state equilibrium geometry.

Ratio	Dipole (d)	Decay (Q)
$\frac{\sigma^*(Q)}{\sigma^*(D)}$	−1.818	2.828
$\frac{\text{Rydberg}}{\sigma^*}$	0.1	0.1

V. DISCUSSION

A. X-ray absorption spectrum

The experimental x-ray absorption spectrum [see Fig. 1(a)] can be roughly divided into two bands: A low energy band which is located below peak 5, and a high energy band above this peak. Peak 5 is identified as a state of Π symmetry compatible with an assignment to the $3p\pi\ ^4\Sigma_u^-$ Rydberg state.[8,15] *Ab initio* calculations show that the latter band arises due to transitions to a manifold of core-excited Rydberg states. We therefore focus our efforts on explaining the fine structure of the low energy band, especially peaks 1, 2, 3, and 4, taking into account earlier work on the oxygen $1s$ absorption spectrum.[5,8,14,15] In a diabatic picture, the first band in Fig. 1(a) is associated with a strong transition to a dissociative core-excited O $1s^{-1}\sigma^*$(D) state.[5] Later,[8,15] the first band was interpreted in the framework of the diabatic approximation as transitions to the bound O $1s^{-1}3s$(Q) Rydberg state simply superimposed on the dissociative band O $1s^{-1}$(D) with no Rydberg-valence mixing.

1. Diabatic model

The set of diabatic curves obtained using this model, displayed in Fig. 4(a), consists of two dissociative curves with a σ^* character crossing a number of Rydberg bound potential curves. Our simulations using the diabatic description in calculations of the XAS presented in Fig. 5(a) do not reproduce the behavior seen in Fig. 1(a) leading us to suggest the following interpretation: The fine structure of the first band is a vibrational structure caused by a bound potential formed by the crossing of the O $1s^{-1}\sigma^*$(Q) and O $1s^{-1}3s$(Q) diabatic curves, while the extensive lower energy tail is due to excitations to dissociative states. The calculated spectrum is dominated by the broad dissociative absorption profiles of the σ^*(Q) and σ^*(D) states (see Table II). The weak Rydberg bands $1s \rightarrow 3s$(D) and $1s \rightarrow 3s$(Q) arising from the shallow potentials in Fig. 4(a) have widths of about 0.3–0.5 eV, and a vibrational spacing of about 0.17 eV. Comparison with the experimental spectrum shows that this model is clearly not satisfactory.

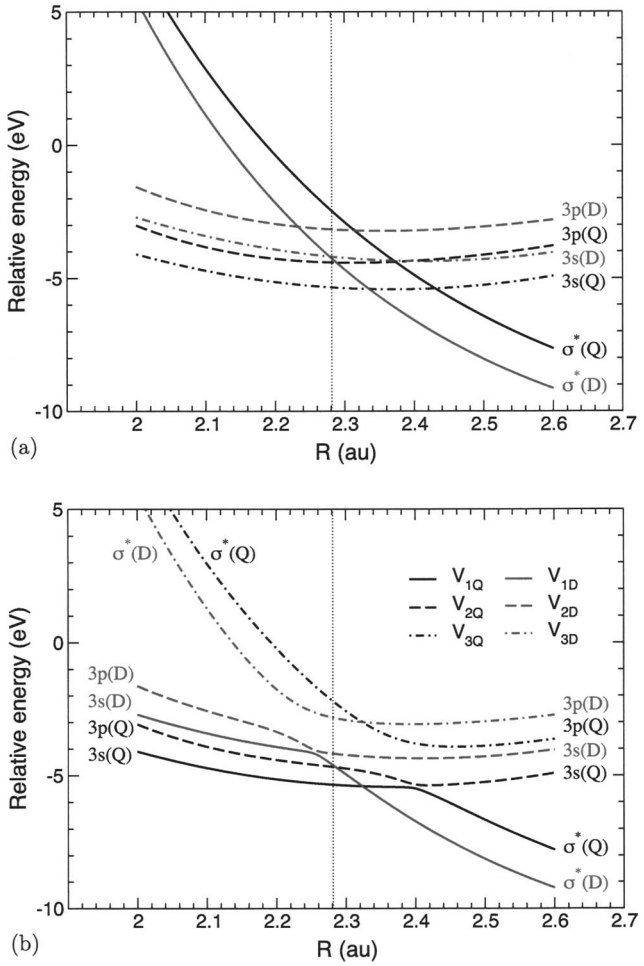

FIG. 4. (a) Diabatic potential curves calculated as discussed in the text (cf. Sec. IV B); (b) Mixed adiabatic/diabatic potential curves of the four-crossing model. The vertical dotted line indicates R_{eq} of the ground state.

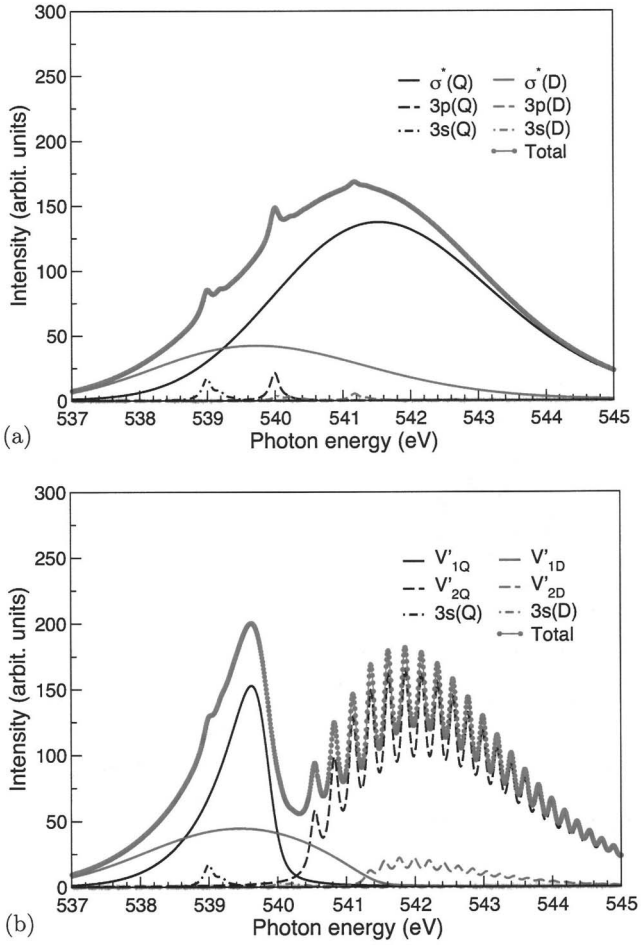

FIG. 5. (a) Theoretical x-ray absorption spectrum based on the diabatic model; (b) theoretical x-ray absorption spectrum based on the two-crossing model. (see text for further explanations). The absolute theoretical energy scale was shifted by about +1.0 eV in order to match the experimental spectrum.

2. Two-crossing model

Implementation of this model significantly improves the accuracy of the computed x-ray absorption profile, as shown in Fig. 5(b). The spectrum exhibits two bands, although the fine structure of the low energy band does not match the experimental spectrum exactly, and the higher-energy band is, as expected from the limits of the model, rather different from the experiment. The general similarity of the low energy band is, however, encouraging, and we observe that its peculiar shape arises from a transition to the V'_{1Q} state: The absorption is suppressed in the region with predominant $3p$(Q)-Rydberg character, while it is enhanced in the region dominated by the σ^*(Q) [V'_{1Q} is similar to V_{1Q} in Fig. 4(b)].

3. Four-crossing model

The theoretical x-ray absorption profile based on the four-crossing model reported in Fig. 1(b) shows the best agreement with the experimental low energy band, even though the wave-packet dynamics is not strictly correct. However, our neglecting of the vibronic coupling primarily affects the intensity ratios within the spectrum rather than the exact peak positions. The model can be discussed on the basis of the following points:

(i) The avoided crossing of the diabatic potentials σ^*(Q) and $3s$(Q) forms a bound potential V_{2Q} which, in agreement with the experiment, has large vibrational frequencies. This is due to the fact that the adiabatic potential V_{2Q} is steeper than the diabatic potential $3s$(Q) [compare Figs. 4(a) and 4(b)]. The energy separation between peaks 1, 2, and 3, and 4 is 0.30, 0.27, and 0.20 eV.

(ii) The positions of peaks 1, 2, 3, and 4 in the experiment agree remarkably well with the vibrational progression of the bound adiabatic state V_{2Q}. The first three peaks correspond to the vibrational levels inside the "deep" part of potential V_{2Q} on the right side of R_{eq} [see Fig. 4(b)]. For $R<2.35$ a.u., the $3p$(Q)-Rydberg state gradually becomes dominant causing an "opening" of the V_{2Q} potential. Thus, the spacing between peaks 3 and 4 is diminished [cf. Fig. 1(b)].

(iii) The experimental intensity distribution between peaks 1, 2, and 3 is not reproduced by the simulation; it is plausible that this is the result of vibronic coupling. We expect that the higher-energy peaks 2 and 3 should be affected by vibronic coupling. In principle, vibronic coupling results in a transfer of the nuclear

wave packet from the bound potential to the dissociative potential curve [cf. Fig. 4(b)] and, under certain conditions, the wave packet can escape completely.

In the simulation we take several experimentally derived parameters into account. The nominal resonance energy is used to define the detuning frequency in the theoretical calculation,

$$\Omega = \omega - \omega_{\text{top}}. \tag{8}$$

We assume that the energy ω_{top} is defined by the first sharp peak in the experimental absorption spectrum at 538.95 eV. The energy of the vertical transition to the potential V_{1Q} in Fig. 4(b) is 0.17 eV below this peak. We find that the most important states are the adiabatic continuum states (V_{1Q} and V_{1D}). Let us stress that, due to the limited number of excited states included in our present theoretical model, the simulation of the high energy absorption band ($E_{\text{ph}} > 540.5$ eV) cannot be considered accurate enough.

B. Role of vibronic coupling

Thus far, we have neglected vibronic coupling, but it may be included roughly in a simplified approach based on the Landau-Zener (LZ) theory.[47] First we need the probability of a wave packet to propagate along an adiabatic potential,

$$\varpi_\nu = 1 - P_\nu, \quad P_\nu = \exp[-(\beta/\beta_c^{(\nu)})^2], \tag{9}$$

where β_c the critical electronic coupling between diabatic states 1 and 2,

$$\beta_c^{(\nu)} = \sqrt{\frac{v_\nu |f_1 - f_2|}{2\pi}}, \quad v_\nu = \sqrt{\frac{\epsilon_\nu}{\mu}}. \tag{10}$$

The speed of the relative nuclear motion in the vibrational state ν is expressed through the reduced mass μ and vibrational energy ϵ_ν in an adiabatic potential. Here, $f_i = dV_i/dR$ is the derivative of the diabatic potential $V_i(R)$ at the crossing point R_c. In the present case, the indices 1 and 2 denote diabatic potentials of the states $\sigma^*(Q)$ and $3s(Q)$. Vibronic coupling is included by multiplying the intensity of each vibrational peak in the adiabatic approximation σ_ν^{ad} by ϖ_ν,

$$\sigma_\nu^{\text{ad}} \rightarrow \varpi_\nu \sigma_\nu^{\text{ad}}. \tag{11}$$

We estimate that $\beta_c^{(0)} = 0.0064$ a.u., a value that is 2.6 times larger than the value used to divide crossing points in the "diabatic" and "adiabatic" ones. Using that value, we obtain ratios $\beta/\beta_c^{(\nu)}$ which overestimate the probability P_ν of the diabatic propagations. However, we have already established that the diabatic picture does not match the experiment [cf. Fig. 5(b)], so we increase the ratio $\beta/\beta_c^{(\nu)}$ by a factor of 2 and assume that $\beta_c^{(0)} = 0.0032$ a.u. The simulation in Fig. 6 based on Eq. (11) show much better agreement with the experimental data in Fig. 1(a) than the XAS profile computed within the adiabatic picture in Fig. 1(b). We conclude that vibronic coupling indeed inverts the intensity distribution of the adiabatic vibrational progression. The reason for this is that the probability to follow the adiabatic potential ($\varpi_0 = 0.68$, $\varpi_1 = 0.41$, $\varpi_2 = 0.34$, and $\varpi_3 = 0.31$) decreases for higher vibrational states because the wave packets move faster. We would like to point out that this interpretation, based on physical intuition, only provides an estimation of the nondiabatic coupling effect on the vibrational peaks.

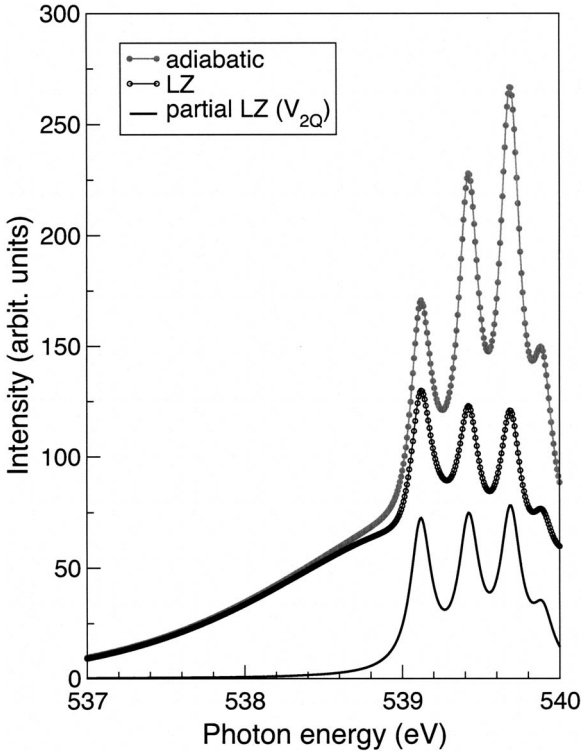

FIG. 6. Estimate of vibronic coupling (VC) effect in the four-crossing model. The partial vibrational profile [marked as "partial LZ (V_{2Q})"] is weighted by Landau-Zener (LZ) probabilities ϖ_ν [cf. Eq. (9)] of propagation in the bound adiabatic V_{2Q} state. The labels "adiabatic" and "LZ" mark total XAS spectra computed in adiabatic approximation and taking into account the LZ factor ϖ_ν; $\beta_c^{(0)} = 0.0032$ a.u.

C. Resonant Auger scattering spectra

Now that we have calculated the excited-state potential curves, we are in a position to examine in detail the experimental resonant Auger electron spectra [cf. Fig. 2(a)] and to evaluate further the models describing the coupling between the intermediate state potential energy curves. The ground and final electronic states are usually very well known and, in the case of molecular oxygen, the singly ionized X state is relatively well separated from the ionic A state, with about a 4 eV binding energy gap. For the interpretation of the Auger spectra, the propagation of the excited-state wave packet must be included in the simulation and the resonant and nonresonant channels must be considered.

We simulate the spectra using RAS wave-packet dynamics based on a highly successful formalism which has been extensively used in calculations in molecules.[29] The cross section for x-ray absorption is

$$\sigma(\omega) \propto \sum_{i\alpha} \sum_{\nu_{i\alpha}} \frac{\langle \nu_{i\alpha} | d_{i\alpha}^{\text{ad}}(R) | 0 \rangle^2 \Gamma}{(\omega - \omega_{i\nu_{i\alpha},0})^2 + \Gamma^2}, \tag{12}$$

and of the RAS,

$$\sigma(\mathrm{BE},\omega) \propto \sum_{\nu_f} \frac{|F_{\nu_f}|^2 \Gamma_f}{(\mathrm{BE}-\omega_{f\nu_f,0})^2+\Gamma_f^2}, \quad \mathrm{BE}=\omega-E, \tag{13}$$

and is accurate within a constant. Here, $|0\rangle$, $|\nu_{i\alpha}\rangle$, and $|\nu_f\rangle$ are the vibrational states of the ground, core-excited, and final electronic states, respectively, and $\omega_{i\nu_{i\alpha},0}$ and $\omega_{f,0}$ are the frequencies of the resonant transitions from the ground to the core-excited and final states. The binding energy $\mathrm{BE}=\omega-E$ is the difference between the frequency of the incident photon (ω) and the kinetic energy of the Auger electron (E). The spectral profile depends on the lifetime broadening of the core-excited [half width at half maximum (HWHM) $\Gamma=0.08$ eV] and final (HWHM $\Gamma_f=0.01$ eV) states. The scattering amplitude consists of resonant and nonresonant contributions,

$$F_{\nu_f} = A\langle\nu_f|0\rangle + \sum_{i\alpha}\sum_{\nu_{i\alpha}} \frac{\langle\nu_f|Q_{i\alpha}^{\mathrm{ad}}(R)|\nu_{i\alpha}\rangle\langle\nu_{i\alpha}|d_{i\alpha}^{\mathrm{ad}}(R)|0\rangle}{\omega-\omega_{i\nu_{i\alpha},0}+i\Gamma}. \tag{14}$$

The amplitude of the nonresonant channel A is proportional to the dipole moment for direct ionization of the $1\pi_g$ electron.

The fast scattering limit is an important benchmark[19] obtained for large frequency detuning $\Omega=\omega-\omega_{\mathrm{top}}$, so that

$$\tau\omega_{\mathrm{vib}} \gg 1, \quad \tau\beta \gg 1, \quad \tau=\frac{1}{\sqrt{\Omega^2+\Gamma^2}}, \tag{15}$$

where ω_{top} is the peak position of the x-ray absorption profile. During the period $1/\beta$, the crossing diabatic states are mixed resulting in adiabatic states. These states can be further mixed through the vibronic coupling interaction V_{VC}. The result is that near the crossing points the interaction dynamics between the states is characterized by three "times," $1/\beta$, $1/|V_{\mathrm{VC}}|$, and the period of vibrations $1/\omega_{\mathrm{vib}}$, where ω_{vib} is the frequency of molecular vibrations leading to vibrational coupling.

In the present case, the interference between electronic and vibrational states is highly relevant. Due to the completeness of the set of vibrational states $|\nu_i\rangle$ of the electronic core-excited states, and because the transformation matrix $c=c_{i,n(\alpha)}$ is unitary,

$$\sum |\nu_i\rangle\langle\nu_i| = 1, \quad c^\dagger c = 1. \tag{16}$$

The scattering amplitude [cf. Eq. (14)], in the limit of fast scattering, becomes,[19,27,44,45]

$$F_{\nu_f} = \left(A + \frac{1}{\Omega+\imath\Gamma}\sum_{\alpha,n(\alpha)} Q_{n(\alpha)}^{\mathrm{diab}} d_{n(\alpha)}^{\mathrm{diab}}\right)\langle\nu_f|0\rangle. \tag{17}$$

This implies that the resonant Auger scattering profile is identical to the vibrational profile for direct photoionization. The interference of electronic states is crucial since in this limiting case alone [cf. Eq. (15)], the transition moments d and Q become independent of R so that the vibrational profile depends solely on the overlap of the ground and final vibrational states.

Our simulation employed the time-dependent representations for the cross sections according to Eqs. (12)–(14). Following the method outlined in Ref. 28, we obtain the following expression for the x-ray absorption cross section:

$$\sigma(\omega) = \Re\sum_{i(\alpha)} \int_0^\infty \sigma_{i(\alpha)}(t) e^{\imath(\omega+\imath\Gamma)t} dt,$$
$$\sigma_{i(\alpha)}(t) = \langle 0|\varphi_{i(\alpha)}(t)\rangle, \tag{18}$$

and for the resonant Auger scattering cross section for narrow-band monochromatic excitation,

$$\sigma(\mathrm{BE},\omega) = \Re\int_0^\infty C_f(\tau) e^{\imath(\mathrm{BE}+\imath\Gamma_f)\tau} d\tau. \tag{19}$$

The nuclear wave packets in the core-excited ($|\varphi_i(t)\rangle$) and final state ($|\varphi_f(t)\rangle$) potential curves,

$$|\varphi_{i(\alpha)}(t)\rangle = e^{-\imath(H_{i(\alpha)}-E_0)t} d_{i,\alpha}|0\rangle, \quad |\varphi_f(t)\rangle = e^{-\imath(H_f-E_0)t}|0\rangle, \tag{20}$$

determine the resonant Auger scattering amplitude and its direct contribution. Here, H_i and H_f are the nuclear Hamiltonians of the core-excited and final states. The resonant Auger scattering channel amplitude is given by the half-Fourier transform of the autocorrelation function

$$C_f(\tau) = |A|^2\langle 0|\varphi_f(\tau)\rangle + \imath\{A\langle\Psi(0)|\varphi_f(\tau)\rangle - A^*\langle 0|\Psi_f(\tau)\rangle\} + \langle\Psi(0)|\Psi_f(\tau)\rangle, \tag{21}$$

which is the sum of the direct contribution, the interference between the direct and resonant scattering channels, and the resonant term. The dynamics of the resonance and interference scattering depend on the wave packets,

$$|\Psi_f(\tau)\rangle = e^{-\imath(H_f-E_0)t}|\Psi(0)\rangle,$$
$$|\Psi(0)\rangle = \sum_{i\alpha} Q_{i\alpha}\int_0^\infty e^{-\imath(H_{i(\alpha)}-E_0-\omega)t} d_{i,\alpha}|0\rangle dt. \tag{22}$$

Here, $H_f=T+V_f(R)$ and $H_{i(\alpha)}=T+V_{i(\alpha)}(R)$ are the nuclear Hamiltonians with potentials $V_f(R)$ and $V_{i(\alpha)}(R)$, $E_0=V_0(R_0)+\omega_0/2$, where ω_0 is the ground-state vibrational frequency. We performed simulations both in the mixed adiabatic/diabatic models and the diabatic model ($d_{i,\alpha}=d_{i,\alpha}^{\mathrm{ad,diab}}$, $Q_{i,\alpha}=Q_{i,\alpha}^{\mathrm{ad,diab}}$).

The simulation of the decay spectra tests the effect of intermediate states interaction on the potential curves, the dynamic model for wave-packet propagation and the role of vibrational coupling to a high degree. We made a systematic study of the decay to the X state where the core-excited states are handled as described above in the diabatic, the two-crossing, and the four-crossing models. In addition, the role of the direct photoionization channel and interference are taken into account as described above.

1. Diabatic model

Although the diabatic model did not reproduce the experimental x-ray absorption profile successfully (cf. Sec. V A), it may offer useful information about the experimental resonant Auger scattering profile since all of the crossing points except the lowest one in Fig. 4(a) lie above the ex-

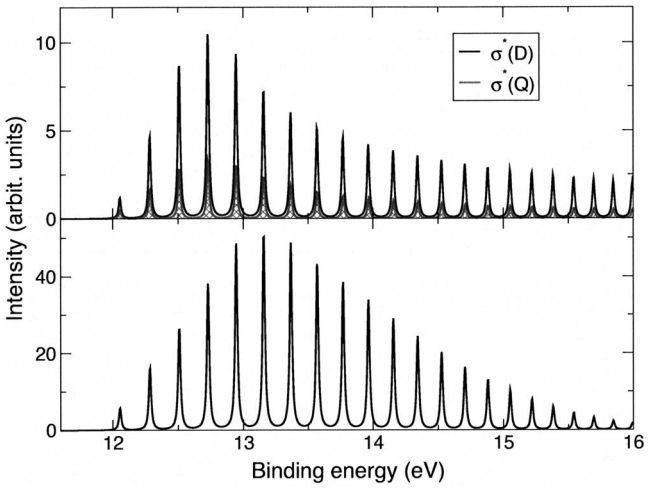

FIG. 7. Comparison of the partial resonant Auger scattering cross sections $\sigma^*(D)$ and $\sigma^*(Q)$ (upper panel) with the total cross section which includes the interference term (lower panel) for detuning, $\Omega=-0.68$ eV [cf. experimental spectrum C from Fig. 2(a)]. The direct photoionization channel is not included.

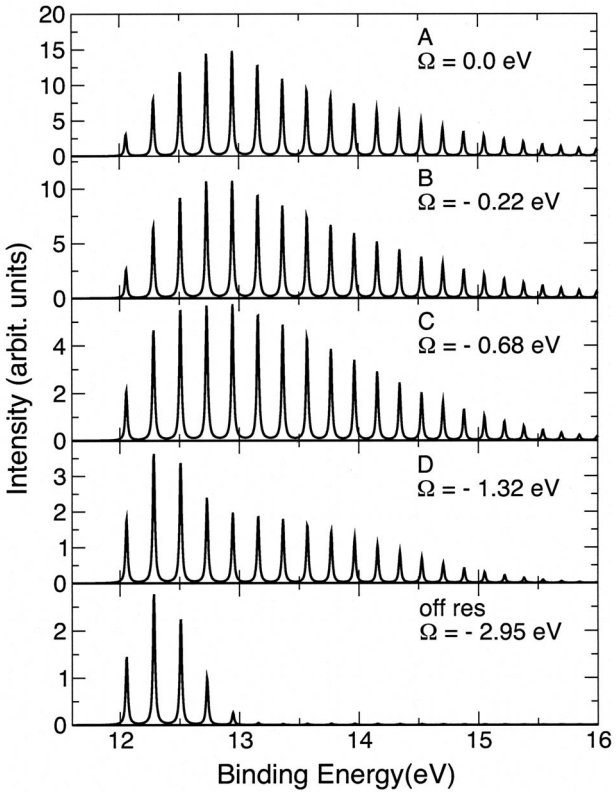

FIG. 8. Total resonant Auger scattering cross sections where the direct channel is included, $A=20$, $\phi=0$.

perimental excitation energies. The electronic interaction β at the lowest crossing point, $\beta(\sigma^*(Q)|3s(Q))$ (cf. Table I) is small enough to cause a small difference between the diabatic model and the adiabatic one. The resonant Auger scattering profile in the diabatic model derives mainly from the two core-excited states $\sigma^*(Q)$ and $\sigma^*(D)$. The most striking experimental RAS spectrum is spectrum C in Fig. 2(a) where the peak intensities vary in an unusual pattern. The simulations using the diabatic model for scattering at this energy ($\Omega=-0.68$ eV) are shown in Fig. 7 where the quartet and doublet channels are plotted separately in the upper panel, and the sum including interference is shown in the lower panel. In the calculation shown in Fig. 8, we include the direct ionization channel, and take interference between the resonant and direct channels into account ($A=20$ a.u., $\phi=0°$). Although these simulations reproduce to some extent the gross features of the experiment, the oscillations observed in spectrum C of Fig. 2(a) are not visible.

2. Two-crossing model

The considerations presented for the diabatic model apply for this case as well. The lowest crossing included in the two-crossing model is between the $\sigma^*(Q)$ and $3p(Q)$-Rydberg states. It is situated about 1 eV higher than the crossing between the $\sigma^*(Q)$ and $3s(Q)$-Rydberg states, i.e., far above $\omega_{top}=538.5$ eV. Therefore, the two-crossing model would produce results which do not differ considerably from the diabatic model. This conclusion is in accord with simulations which are not shown here.

3. Four-crossing model

Fig. 2(b) shows the results of simulations using the four-crossing model with $A=60$ a.u., $\phi=100°$ which produce the best agreement with the measurement in Fig. 2(a). The real amplitude of the direct channel ($A=20$ a.u., $\phi=0°$) used in the diabatic model calculations produces spectra which show a slightly worse agreement with the experimental data than the profiles shown in Fig. 2(b). We used a complex amplitude[46] $A \rightarrow A\exp(i\phi)$ for the direct channel ($A=60$ a.u., $\phi=100°$), in order to improve the agreement.

The theoretical resonant Auger scattering spectra in Fig. 2(b) show excellent agreement with the off-resonant case, and for the case of spectrum D. In spectrum C, apart from the minimum around peak 4, one can distinguish local minima at peaks 9 and 11, which are also in accord with the experimental intensities. While the first minimum is due to the interference with the direct term, we cannot give a clear explanation for the other minima.

There is some disagreement between experiment and theory for spectra A and B. The measured spectrum A resembles the calculated spectrum B, but the intensity maximum at vibrational peak 7 is not reproduced in the calculation. This is most likely due to the error introduced in the adiabatic limit of the treatment of the lowest crossing between the $\sigma^*(Q)$ and $3s(Q)$-Rydberg states, by neglect of vibronic coupling. In the four-crossing model near the top of the resonance, the absorption to the bound adiabatic state V_{2Q} is enhanced. In Sec. V A we noted that the intensities of the vibrational peaks are overestimated by the four-crossing model. The reason for this is the perfect localization of the nuclear wave packet in the V_{2Q} bound potential in Fig. 4(b). This vertical transition to the final state leads to an abnormally strong band between 12 and 13 eV binding energy [see spectra A and B in Fig. 2(b)]. In a more realistic model which includes vibronic coupling, parts of the wave packet trapped in the V_{2Q} well would be expected to escape into the

dissociative state V_{1Q}. This would lead to increased decay transitions for the higher vibrational levels, as it is observed in the experiment.

VI. SUMMARY

The x-ray absorption and resonant Auger electron spectra of molecular oxygen were studied both experimentally and theoretically in the O $1s \rightarrow \sigma^*$ excitation region, which represents a unique example of a comparatively simple molecule with multiple crossings of core-excited state potential curves. Due to these curve crossings, the Born-Oppenheimer approximation breaks down, invalidating the applicability of the diabatic picture for the description of the spectral shape of this part of the x-ray absorption profile. Based on these findings, the fine structure in this spectral region has been assigned for the first time to bound Rydberg states with a surprisingly large vibrational spacing. Our numerical simulations are based on a mixed adiabatic/diabatic picture which classifies crossing points according to the strength of the electronic coupling. A wave-packet technique for the nuclear dynamics in these core-excited states was adopted for the calculation of the Auger spectra, where the interference of the resonant scattering channels through different core-excited electronic states as well as the interference between the direct and resonant channels were accounted for. We find that the long vibrational progression of the $X\,^2\Pi_g$ state is mainly due to the decay of dissociative core-excited states. The overall agreement between the experimental Auger spectra and the calculation supports the mixed diabatic/adiabatic picture, but it can be expected that the computed vibrational intensity distribution could be improved by the inclusion of non-adiabatic coupling in the model.

ACKNOWLEDGMENTS

This work was supported by the Swedish Research Council (VR), the Foundation for Strategic Research (SSF), and by the Swedish Foundation for International Cooperation in Research and Higher Education STINT. The experiments were carried out with the approval of JASRI and supported in part by Grants in aid for Scientific Research from the Japanese Society for the Promotion of Science. We are grateful to the staff of SPring-8 for assistance during the measurements. R.F., F.G., and V.C. acknowledge support and hospitality from Tohoku University during their stay in Japan, where essential parts of the work was carried out. The present investigation is part of the Research Project No. MD-P08-IPCF-C3 of IPCF-CNR and it has been also financed by the local funds of the University of Ferrara.

[1] A. P. Hitchcock and C. R. Brion, J. Electron Spectrosc. Relat. Phenom. **18**, 1 (1980).
[2] W. Wurth, J. Stöhr, P. Feulner, X. Pan, K. R. Bauchspiess, Y. Baba, E. Hudel, G. Rocker, and D. Menzel, Phys. Rev. Lett. **65**, 2426 (1990).
[3] M. W. Ruckman, J. Chen, S. L. Qui, P. Kuiper, and M. Strogin, Phys. Rev. Lett. **67**, 2533 (1991).
[4] Y. Ma, C. T. Chen, G. Meigs, K. Randall, and F. Sette, Phys. Rev. A **44**, 1848 (1992).
[5] N. Kosugi, E. Shigemasa, and A. Yagishita, Chem. Phys. Lett. **190**, 481 (1992).
[6] M. Neeb, J.-E. Rubensson, M. Biermann, and W. Eberhardt, Phys. Rev. Lett. **71**, 3091 (1993).
[7] P. Kuiper and B. I. Dunlap, J. Chem. Phys. **100**, 4087 (1994).
[8] A. Yagishita, E. Shigemasa, and N. Kosugi, Phys. Rev. Lett. **72**, 3961 (1994).
[9] H. Ågren, L. Yang, V. Carravetta, and L. G. M. Pettersson, Chem. Phys. Lett. **259**, 21 (1996).
[10] A. Kivimäki, B. Kempgens, M.-N. Piancastelli, M. Neeb, K. Maier, A. Rüdel, U. Hergenhahn, and A. M. Bradshaw, J. Electron Spectrosc. Relat. Phenom. **93**, 81 (1998).
[11] M. Coreno, M. de Simone, K. C. Prince, R. Richter, M. Vondraćek, L. Avaldi, and R. Camilloni, Chem. Phys. Lett. **306**, 269 (1999).
[12] M.-N. Piancastelli, A. Kivimäki, V. Carravetta, I. Cacelli, R. Cimiraglia, C. Angeli, H. Wang, M. Coreno, M. de Simone, G. Turri, and K. C. Prince, Phys. Rev. Lett. **88**, 243002 (2002).
[13] N. Kosugi, Chem. Phys. **289**, 117 (2003).
[14] I. Hjelte, O. Björneholm, V. Carravetta, C. Angeli, R. Cimiraglia, K. Wiesner, S. Svensson, and M.-N. Piancastelli, J. Chem. Phys. **123**, 064314 (2005).
[15] J. Adachi, N. Kosugi, and A. Yagishita, J. Phys. B **38**, R127 (2005).
[16] S. L. Sorensen, T. Tanaka, R. Feifel, J. H. D. Eland, M. Kitajima, H. Tanaka, R. Sankari, A. De Fanis, M.-N. Piancastelli, L. Karlsson, and K. Ueda, Chem. Phys. Lett. **398**, 168 (2004).
[17] R. Feifel, T. Tanaka, M. Kitajima, H. Tanaka, A. De Fanis, R. Sankari, L. Karlsson, S. Sorensen, M.-N. Piancastelli, G. Prümper, U. Hergenhahn, and K. Ueda, J. Chem. Phys. **126**, 174304 (2007).
[18] S. L. Sorensen, K. J. Borve, R. Feifel, K. Ueda, and A. De Fanis, Chem. Phys. Lett. (submitted).
[19] F. Gel'mukhanov and H. Ågren, Phys. Rep. **312**, 87 (1999).
[20] P. Morin and I. Nenner, Phys. Rev. Lett. **56**, 1913 (1986).
[21] O. Björneholm, M. Bässler, A. Ausmees, I. Hjelte, R. Feifel, H. Wang, C. Miron, M. N. Piancastelli, S. Svensson, S. L. Sorensen, F. Gel'mukhanov, and H. Ågren, Phys. Rev. Lett. **84**, 2826 (2000).
[22] S. L. Sorensen and S. Svensson, J. Electron Spectrosc. Relat. Phenom. **114–116**, 1 (2001).
[23] K. Ueda, J. Phys. B **36**, 1 (2003).
[24] H. Köppel, W. Domcke, and L. S. Cederbaum, Adv. Chem. Phys. **57**, 59 (1984).
[25] K. J. Børve, L. J. Sæthre, T. D. Thomas, T. X. Carroll, N. Berrah, J. D. Bozek, and E. Kukk, Phys. Rev. A **63**, 012506 (2000).
[26] P. Skytt, P. Glans, J.-H. Guo, K. Gunnelin, C. Såthe, J. Nordgren, F. Gel'mukhanov, A. Cesar, and H. Ågren, Phys. Rev. Lett. **77**, 5035 (1996).
[27] A. Cesar, F. Gel'mukhanov, Y. Luo, H. Ågren, P. Skytt, P. Glans, J.-H. Guo, K. Gunnelin, and J. Nordgren, J. Chem. Phys. **106**, 3439 (1997).
[28] P. Salek, F. Gel'mukhanov, and H. Ågren, Phys. Rev. A **59**, 1147 (1999).
[29] P. Salek, Comput. Phys. Commun. **150**, 85 (2003).
[30] F. Kh. Gel'mukhanov, L. N. Mazalov, and A. V. Kondratenko, Chem. Phys. Lett. **46**, 133 (1977).
[31] H. Ohashi, E. Ishiguro, Y. Tamenori, H. Kishimoto, M. Tanaka, M. Irie, T. Tanaka, and T. Ishikawa, Nucl. Instrum. Methods Phys. Res. A **467–468**, 529 (2001).
[32] T. Tanaka and H. Kitamura, Nucl. Instrum. Methods Phys. Res. A **364**, 368 (1995).
[33] T. Tanaka and H. Kitamura, J. Synchrotron Radiat. **3**, 47 (1996).
[34] H. Ohashi, E. Ishiguro, Y. Tamenori, H. Okumura, A. Hiraya, H. Yoshida, Y. Senba, K. Okada, N. Saito, I. H. Suzuki, K. Ueda, T. Ibuki, S. Nagaoka, I. Koyano, and T. Ishikawa, Nucl. Instrum. Methods Phys. Res. A **467–468**, 533 (2001).
[35] Y. Shimizu, H. Ohashi, Y. Tamenori, Y. Muramatsu, H. Yoshida, K. Okada, N. Saito, H. Tanaka, I. Koyano, S. Shin, and K. Ueda, J. Electron Spectrosc. Relat. Phenom. **114–116**, 63 (2001).
[36] H. Yoshida, Y. Senba, M. Morita, T. Goya, A. De Fanis, N. Saito, K. Ueda, Y. Tamenori, and H. Ohashi, AIP Conf. Proc. **705**, 267 (2004).
[37] I. Koyano, M. Okuyama, E. Ishiguro, A. Hiraya, H. Ohashi, T. Kanashima, K. Ueda, I. H. Suzuki, and T. Ibuki, J. Synchrotron Radiat. **5**, 545 (1998).
[38] P. Baltzer, B. Wannberg, L. Karlsson, M. Carlsson–Göthe, and M. Larsson, Phys. Rev. A **45**, 4374 (1992).
[39] V. Carravetta, C. Angeli, and R. Cimiraglia, "Accurate potential curves for the core excited state of O_2" (in press).
[40] B. Huron, J.-P. Malrieu, and P. Rancurel, J. Chem. Phys. **58**, 5745 (1973).
[41] C. Angeli and M. Persico, Theor. Chem. Acc. **98**, 117 (1997).
[42] M. Persico, in *Spectral Line Shapes*, edited by F. Rosta (Walter de

Gruyter and Co., Berlin, 1985), Vol. III.
[43] R. Cimiraglia, J.-P. Malrieu, M. Persico, and F. Spiegelmann, J. Phys. B **18**, 307332 (1985).
[44] F. Gel'mukhanov, T. Privalov, and H. Ågren, Phys. Rev. A **56**, 256 (1997).
[45] S. Sundin, F. Gel'mukhanov, H. Ågren, S. J. Osborne, A. Kikas, O. Björneholm, A. Ausmees, and S. Svensson, Phys. Rev. Lett. **79**, 1451 (1997).
[46] V. Carravetta, F. Gel'mukhanov, H. Ågren, S. Sundin, S. J. Osborne, A. Naves de Brito, O. Björneholm, A. Ausmees, and S. Svensson, Phys. Rev. A **56**, 4665 (1997).
[47] L. D. Landau and E. M. Lifshits, *Quantum Mechanics—Non-Relativistic Theory*, 2nd ed., translated by J. B. Sykes and J. S. Bell (Pergamon, Oxford, 1965).